Earth and Planetary Science Letters 569 (2021) 117062

Contents lists available at ScienceDirect

Earth and Planetary Science Letters

www.elsevier.com/locate/epsl

Intermittent volcanic activity detected in the Von Kármán crater on the farside of the Moon

Yuefeng Yuan [a,*], Peimin Zhu [a,*], Long Xiao [b,*], Jun Huang [b], Edward J. Garnero [c], Jian Deng [a], Fenghua Wang [d], Yuqi Qian [b], Na Zhao [e], Wengang Wang [a], Weiwei Li [a]

[a] Hubei Subsurface Multi-scale Imaging Key Laboratory, Institute of Geophysics and Geomatics, China University of Geosciences, Wuhan 430074, China
[b] State Key Laboratory of Geological Processes and Mineral Resources, Planetary Science Institute, China University of Geosciences, Wuhan 430074, China
[c] School of Earth and Space Exploration, Arizona State University, Tempe, AZ 85287, USA
[d] Institute of Rock and Soil Mechanics, Chinese Academic of Sciences, Wuhan 430071, China
[e] College of Finance & Information, Ningbo University of Finance and Economics, Ningbo 315175, China

ARTICLE INFO

Article history:
Received 10 June 2020
Received in revised form 7 June 2021
Accepted 13 June 2021
Available online 30 June 2021
Editor: W.B. McKinnon

Keywords:
Chang'e-4
lunar penetrating radar
Von Kármán crater
the lunar farside

ABSTRACT

Sensitive to permittivity differences, lunar penetrating radar (LPR) can detect stratification due to material property differences in a medium. We examined the subsurface structures of Von Kármán crater within the South Pole-Aitken (SPA) basin on the farside of the Moon using LPR data obtained by the Chang'E-4 mission. Various distinct strata with depth are clearly recognized, consistent with multiple periods of intermittent lava flows, paleo-regolith, and crater ejecta. Numerous concave and arc shape structures observed at various depths are consistent with buried craters and broken rocks, indicating that the ancient lunar surfaces which are currently buried by up to 30 m deep in Von Kármán, as well as the current surface, suffered numerous impacting events. An imaged subsurface thick paleo-regolith infers a quiescent period with low volcanic activity within the Von Kármán crater. Following the quiescent period (shallower in the profile), a relatively young period of volcanism in the Von Kármán crater is inferred. The mapped stratigraphy and chronology of these events present a self-consistent history of the Von Kármán crater within the SPA, which suggests connections to events on the lunar nearside.

1. Introduction

Unraveling lunar crater subsurface structure is essential for understanding their formation as well as early lunar history. The South Pole-Aitken (SPA) basin, the Moon's largest and oldest impact structure, has a well-preserved impact history, and thus contains essential information for understanding early lunar history of the farside of the Moon (Wilhelms et al., 1987, Head et al., 1993). To investigate this region, China's Chang'E-4 (CE-4) robotic lunar mission (Di et al., 2019) was carried out in the Von Kármán crater inside the SPA (Fig. 1). CE-4 included the Yutu-2 rover to image subsurface structures beneath the mare of the lunar farside using lunar penetrating radar (LPR), which proved effective for exploring the nearside lunar shallow crust in the previous Chang'E-3 mission (Xiao et al., 2015, Yuan et al., 2017, 2020).

The Von Kármán crater formed in the pre-Nectarian period (Losiak et al., 2009, Yingst et al., 2017) from 4.56 to 3.92 Ga (Wilhelms et al., 1987), and is located in the northwestern SPA basin. The reported olivine-rich materials (Li et al., 2020) in the landing region have not been detected so far within the Von Kármán (Huang et al., 2020). The floor of Von Kármán crater experienced several stages of basaltic flooding during the Imbrian period (the 650 Myr that followed the Nectarian) (Wilhelms et al., 1979, Yingst and Head, 1997, Yingst et al., 2017, Pasckert et al., 2018), as well as ejecta delivered from nearby impacts, including that from the creation of Finsen, Alder, Von Kármán L, and the similar-sized Von Kármán L' craters (Huang et al., 2018). However, maria age dating and depositing process analyses in Von Kármán crater differ. For example, Haruyama et al. (2009) deduced a model age for maria in Von Kármán of 3.35 Ga, while the mare units dated by Pasckert et al. (2018) are 3.15 Ga and 3.75 Ga which might be related to younger and older buried flows, respectively. Huang et al. (2018) selected three single geological units in Von Kármán and dated their ages between 3.5 Ga and 3.6 Ga. LPR in the Von Kármán

* Corresponding authors.
E-mail addresses: yuanyf@cug.edu.cn (Y. Yuan), zhupm@cug.edu.cn (P. Zhu), longxiao@cug.edu.cn (L. Xiao).

https://doi.org/10.1016/j.epsl.2021.117062
0012-821X/

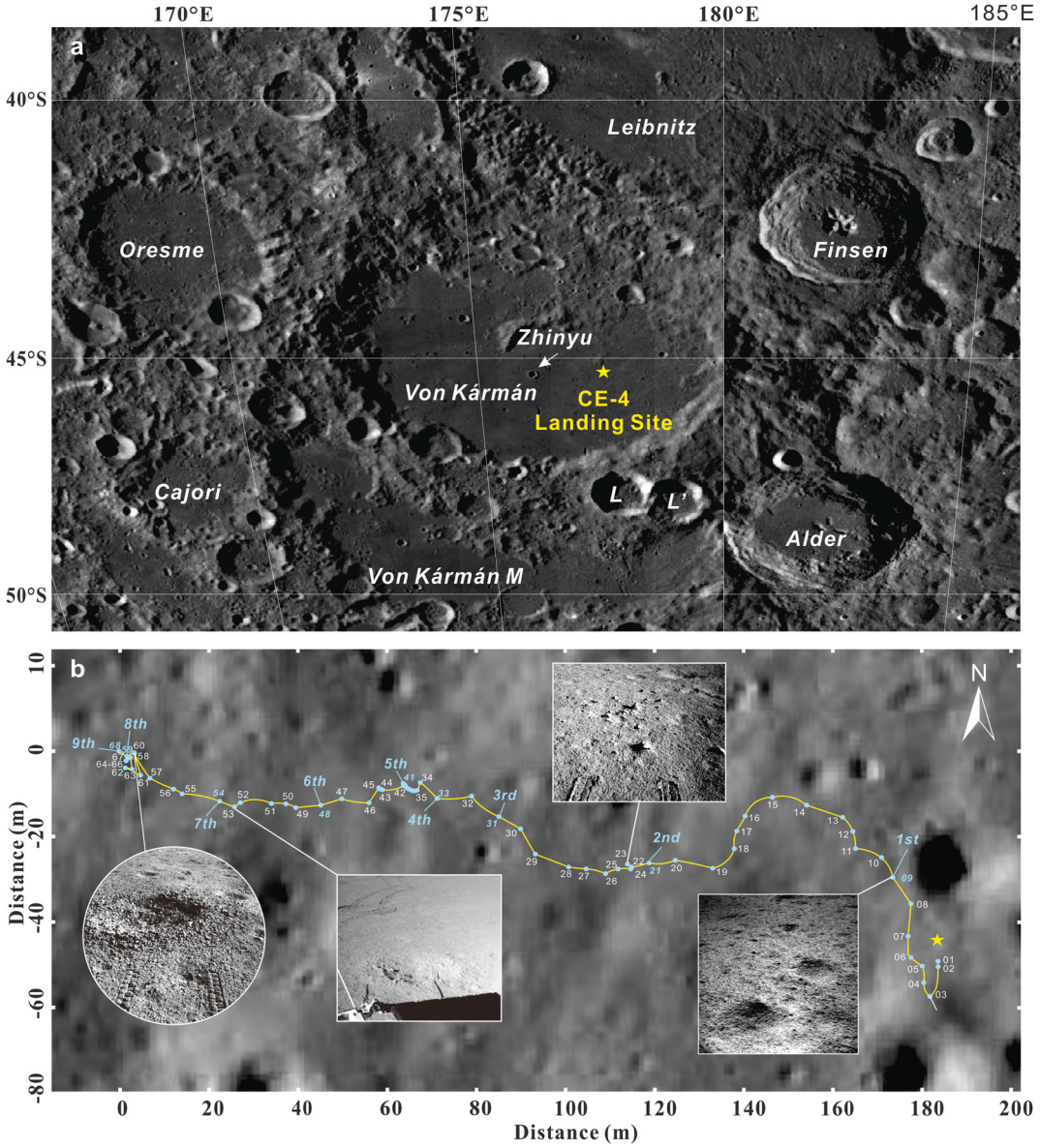

Fig. 1. Chang'E 4 landing site and rover path. (a) Lunar Reconnaissance Orbiter Camera (LROC) Wide-Angle Camera (WAC) mosaic of Von Kármán crater. The yellow star is the landing site of CE-4 (45.46°S, 177.59°E) (Di et al., 2019). (b) Yutu-2 rover path and lunar penetrating radar sites. The Yutu-2 rover path (yellow line) with LPR acquisition locations (blue dots) numbered in order of collection, in the Von Kármán crater. Inset images were taken by the Yutu-2 navigation camera, and display exposed rocks (e.g., locations 23, 53), and local craters (e.g., locations 9, 53, and 60). The distinct Yutu-2 rover wheel tracks (locations 23 and 60) indicate a fine grain regolith. Larger blue text indicates locations of the nine lunar nights. Background image is a LROC Narrow-Angle Camera (NAC) high resolution image (captured from LROC QuickMap, https://quickmap.lroc.asu.edu).

crater can thus directly image the subsurface to better constrain stratigraphy and chronology implied from surface images. Recent LPR studies (e.g. Lai et al., 2020, Zhang et al., 2020a,b) showed several strata interfaces beneath the Yutu-2 surveying path, but the origins of these strata, especially the shallow materials, are not well constrained.

LPR data collected over nine lunar-days are used in this study, and the rover path was traced by photographs from the navigation camera. Yutu-2 was designed to navigate flat surfaces and to explore sites near crater rims as well as diverse types of exposed rocks (Huang et al., 2020). Numerous craters of various diameters were detected along the rover-path from the images of the navigation camera (Fig. 1 and Fig. S1). The distinct imprint left by the wheel of Yutu-2 rover indicates the surface of explored area consists of a fine-grained regolith.

2. Data and methods

2.1. Lunar penetrating radar

The LPR carried by Yutu-2 rover consists of two channels, Channel-1 (CH1) and Channel-2 (CH2), with different center frequencies (60 MHz and 500 MHz, respectively) and bandwidths (40 MHz and 450 MHz, respectively). Their center frequencies correspond to wavelengths of 5 m and 0.6 m in vacuum, respectively. CH1 aims to resolve structures up to hundreds of meters deep with vertical resolution of a few meters, and CH2 focuses on the shallow regolith at the top of lunar surface (uppermost 10's of m) with vertical resolution of 0.15-0.3 m. CH2 has two identical receivers: antenna A and B (CH2A and CH2B, respectively). In this paper, CH2A is not used due to the low quality of data returned from that channel.

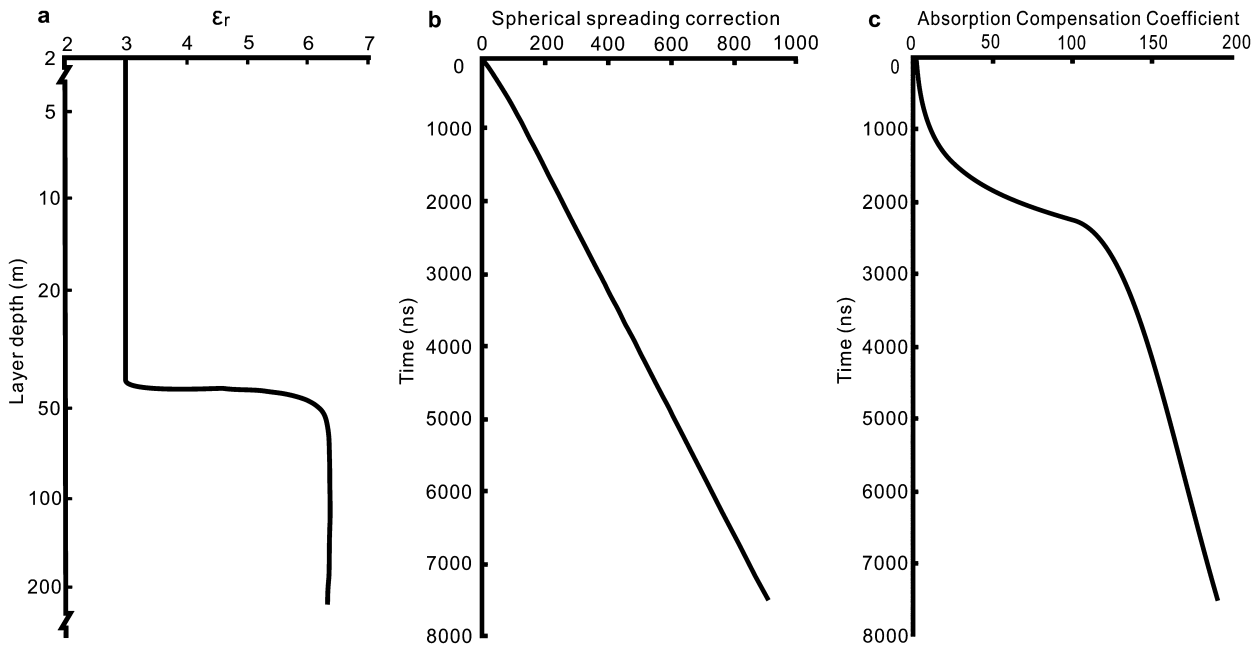

Fig. 2. Parameters for amplitude compensation. (**a**) The relative dielectric constant adopted in this study. (**b**) The time dependency of the spherical spreading correction. (**c**) The time dependency of coefficient (Porcello et al., 1974, Wang et al., 2010) for absorption attenuation compensation.

The LPR sends high-frequency electromagnetic pulses to penetrate the lunar subsurface. For a given position of the LPR on the lunar surface, a radar trace consists of the echoes reflected from subsurface interfaces with contrasting dielectric properties. Thus, all LPR traces along the rover track can be combined together to construct a radar profile, i.e., amplitudes of reflected events versus time, or equivalently, depth below all the positions. The CH1 and CH2B LPR traces are 20480 ns and 640 ns in duration, respectively, with a sampling interval of 2.5 ns and 0.3125 ns, respectively.

2.2. LPR data processing

As the system of navigation and work mode of LPR aboard the Yutu-2 rover is the same as that of Chang'E-3 (CE-3) mission (e.g. Xiao et al., 2015, Yuan et al., 2017, Lai et al., 2019, Li et al., 2020, some of the same inherent problems in the CE-3 LPR data are present in the CE-4 dataset. These include repeated records collected at the same position, unequal spacing between the trace collection locations caused by speed variation of Yutu-2, and interference signals probably generated by electromagnetic coupling with the rover's metallic body (Angelopoulos et al., 2014, Li et al., 2018). We consider and mitigate all of these issues in our data processing to improve the quality of radar profiles constructed from the CH1 and CH2B data (Figs. S2-S8).

Firstly, the LPR waveform variation between adjacent radar traces was measured, resulting in 3368 and 7463 valid traces being selected from the raw LPR data from CH1 and CH2B, respectively, after delay time removing. Radar wave propagation in the subsurface experiences amplitude loss from geometric (spherical wavefront) spreading, as well as absorption (e.g., Xiao et al., 2015). A spherical spreading correction and absorption-attenuation compensation correction were applied to the radar profiles based on the wave propagation distance which is estimated from a dielectric model (Fig. 2). This model was derived from the surface electric experiment at the Apollo-17 site which has a dielectric discontinuity at a depth of ~43 m (Simmons et al., 1973), similar to a shallow interface in our radar profile. We later constrain the dielectric model by wavefield migration tests, and adopt the value 3 as the average relative dielectric constant for the shallow LPR profile.

In the initial profile, uniform horizontal stripes with strong energy signal were present in the upper part of the profile (Fig. S2 and S3), which is likely due to the strong energy of the direct radar wave from the source antenna to the receiver antenna. As those strong amplitude stripes are mainly horizontal, the wave-number filter was designed to remove zero wave number (i.e., horizonal) interferences. A consequence of this filter is that horizontal interfaces along the rover path would not be readily detectable. To reveal distinct deeper structures, noise and inherent interference signals which are dominated in the 5-20 MHz frequency range in CH1 must be removed (as demonstrated with the LPR data in the CE-3 mission by Li et al., 2018). We have thus filtered all LPR traces of the CH1 profiles in the frequency domain with 30-60 MHz bandpass filter. A 200-500 MHz bandpass filter was selected for CH2B after testing. Additionally, a Gaussian smoothing image filter, was applied to sharpen reflections from deep strata.

We further apply the method of Stolt's F-K migration (Stolt, 1978) for CH2B profile to migrate the diffracted waves, whereas migration was not applied to CH1 data as the deeper structures become flatter so that few diffracted waves were recorded. Unequal trace collection location spacing caused by the variation of Yutu-2's speed was also considered by means of migrating separately between the trace collection locations (Fig. S7b). Additionally, the surface relief along the Yutu-2 path can considerably influence mapped interface morphology at depth, especially for shallow structures. Therefore, we correct for the topography on the basis of the relative elevation which is derived from the vertical component of position recorded by LPR (Fig. S7 and S8a). As the radar data is simply approximated to a two-dimensional profile in this paper, the influence of the attitude of the radar antenna is not considered. The resulting lunar radar depth profiles are shown in Fig. 3 (and Fig. S8).

3. Results

We have observed, presented, and interpreted different waveforms in the radar profiles based on the variations in amplitude strength. The strong laterally-extended radar reflection interfaces indicate a dielectric property contrast between regolith/rock or rock/rock materials. According to this pattern, over dozen inter-

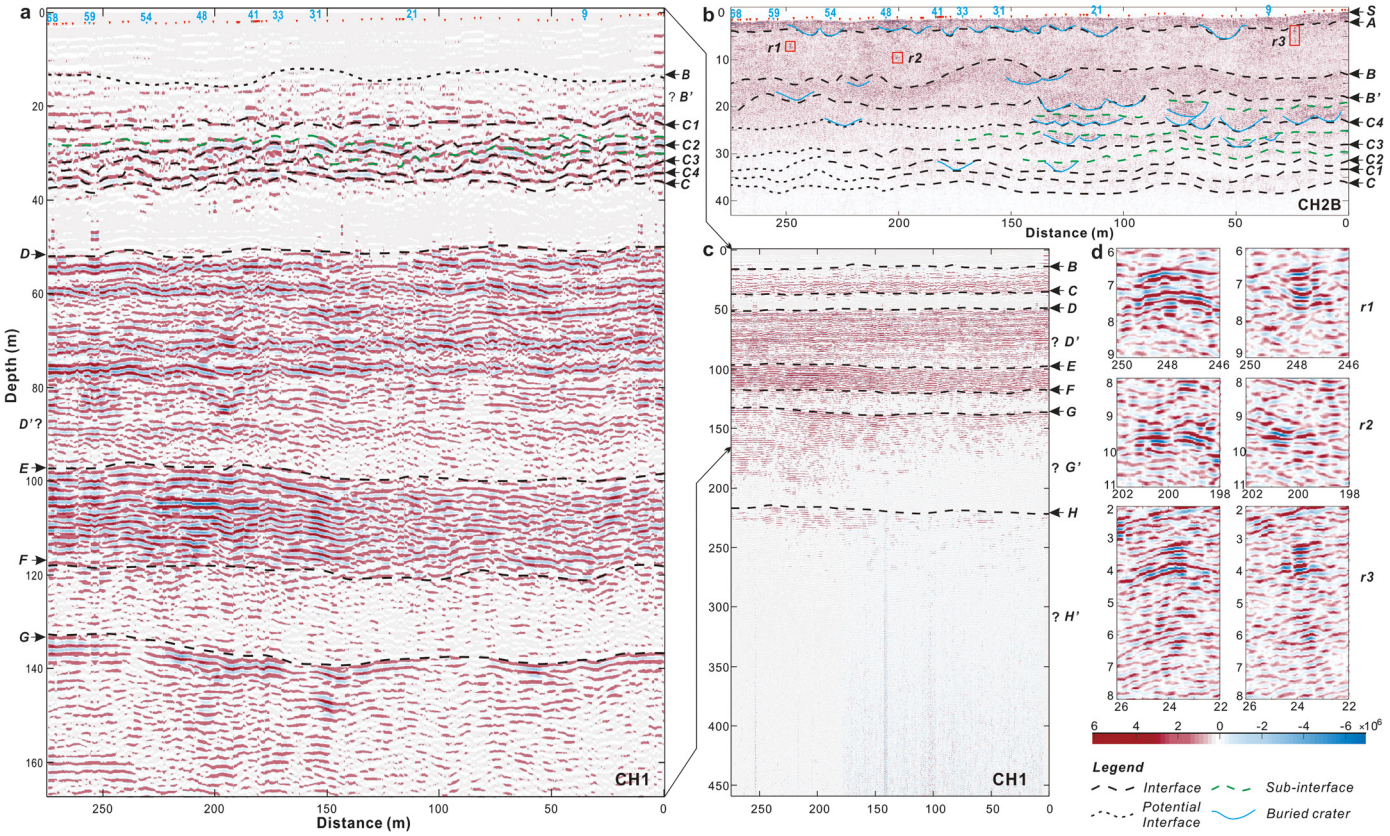

Fig. 3. LPR profiles and subsurface reflectance. (a) The layered subsurface structure along the Yutu-2 path imaged by LPR CH1 data, and (b) CH2B data. The rover progressed from right-to-left in the images, with sites of the 9 lunar nights indicated by the blue numbers at the top of panels (a) and (b) (which correspond to Fig. 1b). The intensity of the red and blue shading, shown as the color scale bar at the right bottom, represents reflectance amplitude strength. Black long-dashed lines outline interfaces which can be tracked continuously across the CH1 and CH2B profiles; green dashed lines demark interfaces that are present in just part of the Yutu-2 path; black short-dashed lines highlight interfaces having high uncertainty. Blue lines indicate clustered reflections of filled concave structures in (b) and may correspond to buried impact craters. (c) An expansion of panel (a) that includes greater depths. (d) Three boxed regions from panel (b) which are zoomed in (***r1***, ***r2***, and ***r3***), exhibiting arc-shaped reflections before migration (left column) and more concentrated structures after migration (right column). All axes are distances in meters.

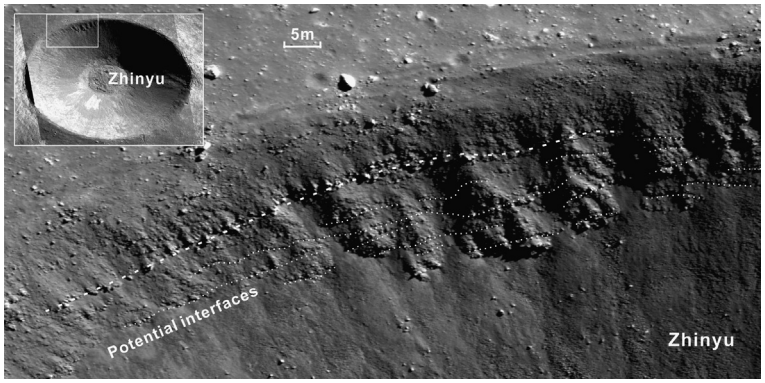

Fig. 4. Exposed lava flow deposition on the rim of Zhinyu crater. The thicker white dashed line delineates an obvious continuous interface with coarse materials. Thinner dashed lines indicate interfaces interpreted as past lava flows. The Zhinyu crater is visible in the center of the Von Kármán crater in Fig. 1, with a diameter of ~3.8 km, which is ~30.8 km away from CE-4 landing site. Roughly 20 m of stratified layers are seen on the crater wall near the rim/surface. (Images were captured from LROC QuickMap, https://quickmap.lroc.asu.edu.)

faces are inferred in LPR profiles (Fig. 3). Terrestrial studies (e.g. Russell and Stasiuk, 1997, Rust and Russell, 2000) demonstrate the efficacy of ground penetrating radar (GPR) for detecting and imaging volcanic sediments (lava flows, pyroclastic rocks, etc.). The LPR profiles presented here thus can similarly map deposits of volcanic origin. Basalt deposits on the lunar surface within the Von Kármán crater exposed in the Zhinyu crater wall (roughly 20 m of stratified layers at the top of the crater, Fig. 4) provide a direct evidence for intermittent superimposed lava flows. This is in good accordance with LPR reflections (Fig. 3), and thus is consistent with an origin of lava flows, pyroclastic rocks, and ejected materials or regolith.

3.1. Profile of LPR CH2B

3.1.1. Shallow layered structures

In the LPR profile of CH2B (Fig. 3b), relatively strong echoes are apparent from the surface (***S***) down to a distinct interface (***A***) that averages ~2.5 m depth, suggesting this surficial layer between ***S*** and ***A*** (hereafter denoted ***S-A***) is surface regolith which has

suffered prolonged impacting. Thus, buried craters along ***A*** were likely filled with ejecta from adjacent craters. Large craters, such as Von Kármán L and L' (Fig. 1a) may have also contributed to the growth of ***S-A*** (each with predicted ejecta blanket thickness less than ~1 m).

Below ***S-A***, reflections in stratum ***A-B*** are relative weak with slight fluctuations of increased reflectance. Buried craters are absent, suggesting contemporaneously deposited materials from the same source. Crater excavation analyses support this, concluding the top materials of the eastern floor of Von Kármán crater contain ejecta from the neighboring Finsen crater (Huang et al., 2018). The depth of ***B*** varies from ~9 to 16 m, consistent with Finsen ejecta thickness estimations at the CE-4 landing site.

Reflectance in stratum ***B-B′*** is stronger than in ***A-B***, with strong and sometimes relatively sharp fluctuations. Diffracted reflections likely caused by broken rocks and/or impact craters are present. Additionally, ***B-B′*** contains large (5-10 m) thickness variations, inferring impact-born ***B*** horizon topography. Reflectance in this stratum is similar to that in surface regolith (***S-A***), and thus may similarly be local regolith, but subsequently interrupted by Finsen ejecta.

Beneath ***B-B′***, multiple distinct reflection interfaces (***C1***, ***C2***, ***C3***, ***C4*** and ***C***) bound ~2-3 m thick layers, consistent with intermittent mare flow deposition. Buried impact craters indicate a paleo Von Kármán crater floor subsequently covered by adjacent crater (and within the Von Kármán crater) ejecta deposits. The family of ***C*** horizon reflections (***C1***, ***C2***, etc.) are reduced in amplitude with depth due to depth-sensitively limitations for CH2B which typically loses resolution below 20 m depth, though some impact craters are visible (Fig. 3b).

3.1.2. Small structures

Two distinctive types of small-scale reflections are apparent. The first is the arc-shaped reflections with strong amplitude variations caused by syncline or concave-shaped reflectors. Fig. 3b shows various concave structures (from ~5 to 20 m in size) over the upper 35 m in depth from surface ***S*** to interface ***C***. The formation of such concave structures is attributed to small impact events from falling projectiles, as opposed to other lunar geological activities, such as space weathering, volcanism, or moonquakes. These inferred buried craters suggest a history of impact events and deposition hiatuses. By analogy, the surface environment traversed by Yutu-2 contains dozens of craters of varying size (diameters from a few to 10's of m, Fig. S1), as well as much larger craters in the greater nearby SPA environment (e.g., Fig. 1). The fact that these buried craters were well preserved indicates that subsequent deposition was relatively rapid, and subsequent geological activities were not to such an extent as to disturb them. These LPR data permit inference on the timing of the depositional rate of an overlaying stratum, and thus provide new information for investigating stratum formation and evolution based on the phenomenon of buried craters.

The second type of distinct small-scale radar reflection is more complex, possessing downward single or double arc-shaped diffractions within layer ***A-B*** which become more concentrated structures following migration processing (***r1***, ***r2***, and ***r3*** in Fig. 3d). Distinct from the concave crater shapes, these structures may correspond to large ejected rocks. Explaining the observed diffractions with buried rocks 2-15 m in size, is supported by synthetic tests of LPR diffractions from buried rock (Zhao et al., 2018) (Fig. S9), and provides new evidence for regolith formation by frequent impacts.

3.2. Profile of LPR CH1

In the LPR profiles of CH1, deeper interfaces (***D-H***) (Fig. 3a and 3c) indicate earlier periods of geological processes contributing to deep mare basement formation within the Von Kármán crater. The CH1 band is designed to explore deep structures with low vertical resolution, thus interfaces in the uppermost 17 m (where ***A***, ***B*** and ***B′*** are detected by CH2B with higher vertical resolution, Fig. 3b) are not resolved, consistent with a relative fine grain size in this depth shell. At greater depths (~17-37 m depth range), strong continuous reflections are observed in the CH1 profile (Fig. 3a), corresponding to strata ***C1***, ***C2***, ***C3***, ***C4*** and ***C*** in the CH2B profile (Fig. 3b).

Stratum ***C-D*** lacks significant reflectance (Fig. 3a), similar to that above interface ***B***, and is thus similarly interpreted as fine-grained paleo-regolith from a hiatus in rapid deposition (of, for example, lava flows). This finding is similar to a quiescent period inferred from a homogeneously weak reflectance layer in LPR data from the Chang'E-3 (CE-3) mission (Yuan et al., 2017) on the nearside of the Moon. Additional weak amplitudes (thus relative fine-grained materials) are apparent in strata ***D′-E***, ***F-G*** (Fig. 3a) and ***G′-H*** (Fig. 3c), though the interfaces ***D′*** and ***G′*** are poorly constrained due to weaker reflectance at these greater depths. Nearly horizontal alternating strong-and-weak reflections in stratum ***D-E*** (Fig. 3a) are interpreted as layered lava flows, similar to those in ***B-C***.

Strong reflections in ***E-F*** (Fig. 3a), however, show interlacing horizontal reflectors, suggesting continuous and relatively rapid material deposition. These reflection patterns are similar to GPR profiles from terrestrial pyroclastic flow deposits (Russell and Stasiuk, 1997), suggesting that some evolutionary processes on the lunar surface may be similar to those on Earth. We can speculate that pyroclastic tephra and tuff are less easily stratified in the lunar vacuum environment, so that sub-paralleled reflections in ***E-F***, and the clear and continuous interface ***E*** are consistent with a subsequent lava flow. Additional evidence from further work will be required to validate this hypothesis.

Deeper interfaces ***G*** and ***H*** feature relative strong reflections at average depths 136 and 222 m, respectively. Associated strata ***G-G′*** and ***H-H′*** possess strong amplitudes and fluctuations similar to ***E-F*** (albeit lower amplitude), but with relatively weak lower interfaces due to limited transmitted energy from these greater depths due to wave attenuation. These reflections can be interpreted as interfaces of early periods of Imbrian lava materials.

3.3. Ejecta of Finsen and Alder crater

The ejecta from large craters adjacent to Von Kármán crater (e.g., Finsen and Alder craters) is expected to be deposited as strata with a thickness which can be estimated by ejecta thickness models (e.g., Sharpton, 2014). Foreign ejecta thickness T can be generally described as $T = aR_t^b(r/R_t)^c$, where r is the distance to the crater center, and R_t is the radius of the transient crater, all in meters, and parameters a, b, and c are constants used to match observed thicknesses (corresponding parameters are shown in Table S1). For large, complex craters, R_t should be estimated from measurable crater properties using a basic geometric model (e.g., Thomson et al., 2009). However, due to the complex original surface located on the rim of large craters, this study simply calculates R_t from $R_t = 0.84R_{SC}^{0.15}R^{0.85}$ (Croft, 1985, Xie et al., 2020) for the complex crater, where $R_{sc} = 9.5$ km is adopted for the transition diameter of simple and complex craters (Pike, 1980), and R is the final rim-to-rim radius. Moreover, the thickness for locally mixed materials is added by μT, where ratio $\mu = 0.0183r^{0.87}$ (for $\mu \leq 5$) (Oberbeck, 1975, Petro and Pieters, 2006). Then we calculate Finsen crater (73 km in diameter) and Alder crater (82

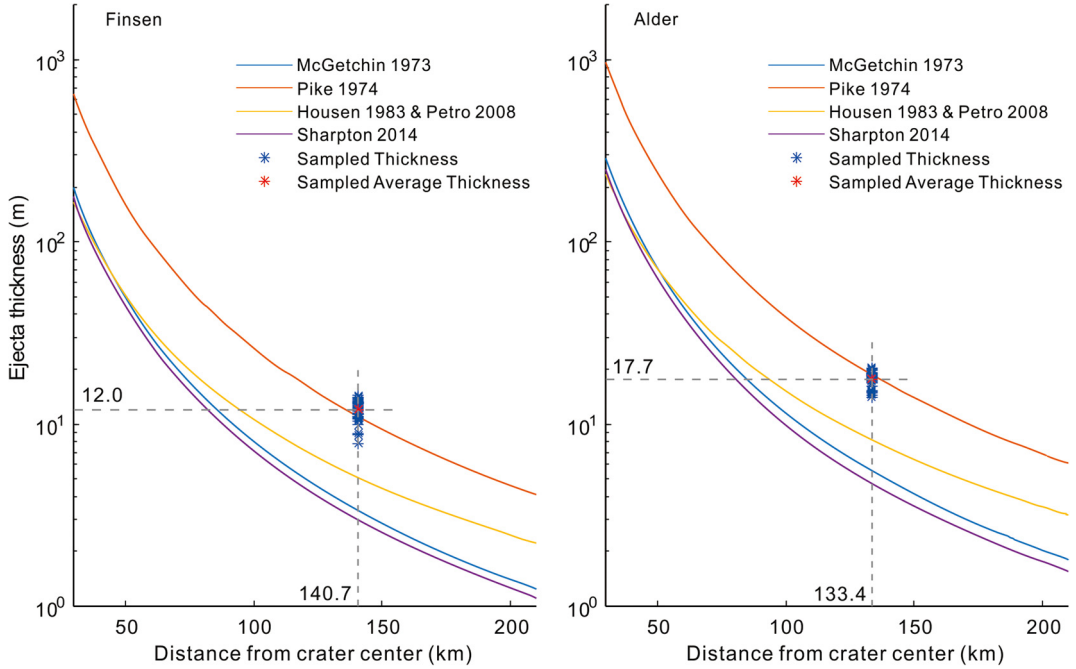

Fig. 5. Thickness predictions of ejecta deposits. The ejecta thickness of (a) Finsen crater and (b) Alder crater, estimated as a function of distance based on different foreign ejecta models (McGetchin et al., 1973, Pike, 1974, Housen et al., 1983, Petro and Pieters, 2008, Sharpton, 2014) after applying a correction for locally mixed materials. The horizontal and vertical gray dashed lines represent distance from the crater center to the CE-4 landing site, and the crater ejecta thickness at CE-4, respectively. The blue asterisks are the observed stratum thicknesses determined from the LPR profile by every 10 m in rover distance, and the red asterisk is their average.

km in diameter) ejecta thicknesses at the CE-4 landing site using different foreign ejecta models (McGetchin et al., 1973, Pike, 1974, Housen et al., 1983, Petro and Pieters, 2008, Sharpton, 2014) together with the correction estimate model of locally mixed materials (Fig. 5). Their crater center to landing site distances is 140.7 km and 133.4 km, respectively.

Finsen crater ejecta includes widespread linear features containing high albedo or surface terrain pointing to Finsen (Huang et al., 2018). The fine-grained Finsen ejecta deposited on the surface is consistent with fine, homogeneous material composing stratum ***A-B***. In contrast, very few radial ejecta features can be traced back to the neighboring Alder crater, suggesting Alder ejecta deposits, which should similarly be fine-grained, have since been buried.

After removing the contribution of crater Von Kármán L and L' (∼2 m in total, Huang et al., 2018), the thickness of Finsen ejecta (inferred to be stratum ***S-B*** in Fig. 2b) around the CE-4 landing site is ∼10 m on average (blue asterisks in Fig. 5(a)), which is consistent with the estimation of the Pike model (Pike, 1974) after the local-mixing correction ($T = 11.0$ m). Moreover, stratum ***F-G*** with weak radar reflections in the LPR profile averages 17.7 m thick (blue asterisks in Fig. 5(b)), which is in good agreement with the estimated thickness of Alder ejecta at the CE-4 landing site using the Pike model ($T = 18.6$ m). The slight differences between observed and estimated thicknesses can be attributed to erosion and compaction of the upper lava flow (as well as ejecta model and radar depth prediction uncertainties). This good accordance of observed and estimated thickness suggests that stratum ***F-G*** was probably formed by ejecta from the Alder crater. Stratum ***G′-H*** is excluded because of its unconstrained top interface.

4. Discussion

4.1. Stratum origins

Fig. 6 displays the Von Kármán crater floor topography, which averages roughly 6000 m below the lunar average, but has significant topographical variations. In order to investigate the origin of these strata, this paper traced topographical variations, flow thicknesses, and flow dips across the CE-4 traverse.

A first-order feature near the CE-4 site is downhill slope to the southwest (along cross-section NN' towards N) and uphill slope to the southeast (along cross-section MM' towards M') that terminates near a dome-like structure (*d*3) near the Von Karman crater wall (near M'). Dome *d*3 contains arc-shaped grooves, and drops ∼80 m over ∼10 km, then an additional 40 m over ∼35 km towards the CE-4 site. The domes are likely expressions of subsurface magmatic intrusion (i.e., laccoliths), possibly with surface extrusion; the location of the dome (*d*3) at the edges of the basin is consistent with earlier flexural loading of the basin by mare deposits (Head and Wilson, 1992, Hiesinger, 2006). Other dome-like units (*d*1, *d*2) exist in the western part of Von Kármán crater (Pasckert et al., 2018, Qiao et al., 2019). Deposits situated downgradient from domes would be consistent with lava flows. As Alder crater shows no evidence for breaching the Von Kármán crater wall (Fig. 1) or flow unit (Stuart-Alexander, 1978), dome *d*3 may have been a dominant source of young lava infilling (i.e., stratum ***B′-C***). Compared to dome *d*3, the northern area (near point M in Fig. 6) is an alternate source of this young lava as there is a downhill slope to the landing site along cross-section MM', and furthermore its location is closer to the CE-4 landing site (though lacking evidence for any structures related to a lava source, e.g., a dome-like unit).

The deepest Von Kármán crater region (-5965 m) corresponds to Imbrian-age lava flow material (Pasckert et al., 2018, Huang et al., 2018), which we interpret as corresponding to stratum ***C-D′*** beneath the CE-4 landing site (we are assuming all dielectric interfaces are flat-lying with respect to surface topography). The deeper imaged strata, ***H-H′***, ***E-F*** and ***D-D′***, show decreasing values (∼3, 2, and 0 m) of average elevation changes across the Yutu-2 path, which intend that the topographical changes of strata become smaller (more and more flat) from deep to shallow. As these stata dip towards the east, we suggest that their materials originated from the west, e.g., from the largest dome-like unit *d*1 in Von Kármán crater (Fig. 6).

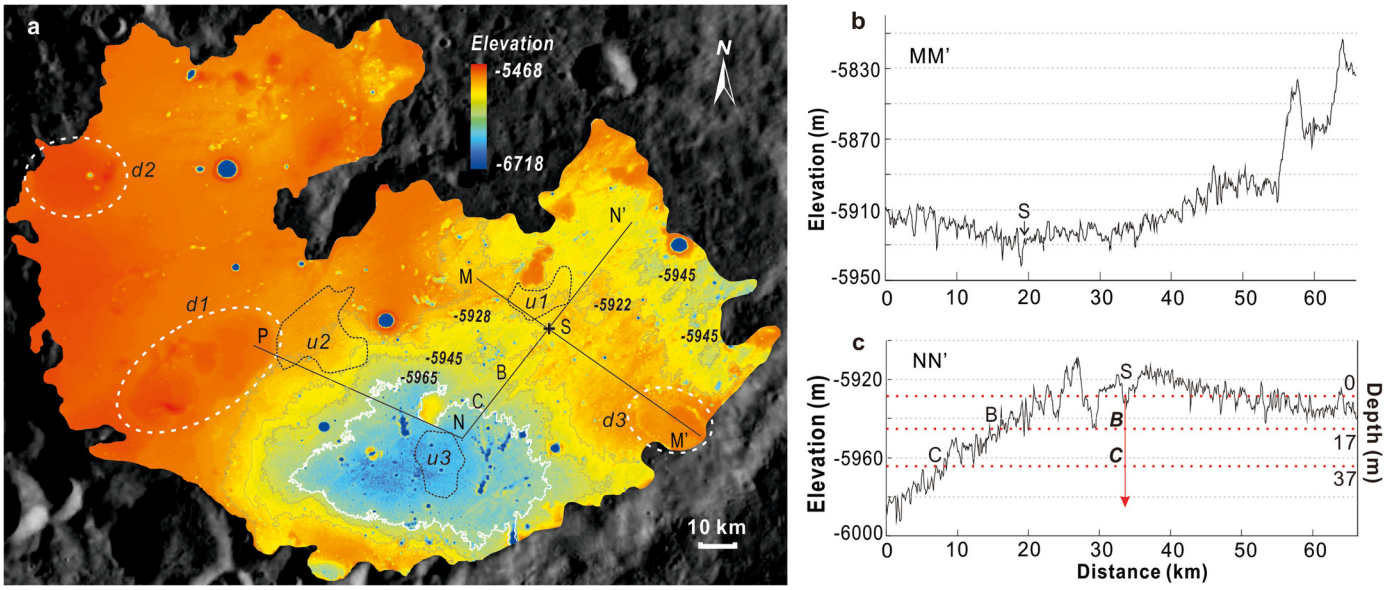

Fig. 6. Topographic profiles near CE-4 landing site. (a) SLDEM2015 topography (Barker et al., 2016) in the Von Kármán crater on a base map image from the LROC Wide-Angle Camera (WAC). The color scale denotes deeper (blue) and shallower (orange, red) elevations. $d1$, $d2$, $d3$ are dome-like units (white dashed ellipses). The ages of mare units $u1$, $u2$ and $u3$ (black dotted regions) were dated in our previous study (Huang et al., 2018). Variable-sized small, dark blue regions are topographical expressions of present-day surface craters. Constant elevation contour lines (white and gray) and associated elevations are shown, with points S, B, and C correspond to the intersection of interfaces ***S***, ***B***, ***C*** (discussed in the text and Fig. 3) with the surface topography. Three cross-section lines are shown, MM', NN', and NP. (b) and (c), Topographic profiles across CE-4 landing site (S) corresponding to MM' and NN' cross-section lines. Horizontal dashed red lines in (c) correspond to the topographical elevations of the CE-4 location (point S), points B and C in (a). We are assuming all dielectric interfaces are flat-lying with respect to surface topography.

4.2. Intermittent lava flows

The low and relatively homogeneous reflectance ***C-D*** stratum (Fig. 3a), interpreted as fine-grained regolith from extended quiescence in section 3.2, is referred to as **Pr3** (for paleo-regolith). Additional potential paleo-regolith layers are observed at 89 and 203 m depth (Fig. 3a and 3c), hereafter, **Pr2** and **Pr1**, respectively (but are poorly constrained due to ambiguous top interfaces). It is noteworthy that the thickness of **Pr3** is ~14 m, significantly exceeding the average thickness of 5 m on lunar maria and 10 m on highland surfaces (Taylor, 1982, McKay et al., 1991). As finest-grain lunar materials are due to continuous space weathering and relatively frequent small impacts, very few large-scale resurfacing events (e.g., lava flows) may have occurred at beneath CE-4 during the formation of **Pr3**. On the other hand, previous work inferred a major peak of volcanic activity between 3.6 Ga and 3.2 Ga within the SPA basin and the crater count in maria Von Kármánis is 3.15 Ga age (Pasckert et al., 2018), suggesting that this thick regolith might have formed after 3.15 Ga, in the early Eratosthenian period. This implies gentle deposition processes during this period, which is in agreement with a quiescent period in the nearside northern Mare Imbrium, from a boundary between the Imbrian and Eratosthenian periods (Yuan et al., 2017). This quiescent period thus infers a low activity of mare volcanism during the early Eratosthenian period.

Following the inferred quiescence period, the ***B-C*** stratum deposited above the ***C-D*** stratum may correspond to the second peak of volcanic activities (hereafter, **Em**, for Eratosthenian mare unit) on the lunar farside between 2.2-2.5 Ga (Haruyama et al., 2009, Pasckert et al., 2018). Then the observations of this mare-like stratum suggest a new, younger period of volcanic activity within Von Kármán crater.

The LPR profile presented here suggests the scale of farside lava flows is similar to those on the nearside (Xiao et al., 2015, Yuan et al., 2017). For example, evidence for relatively thin (2-10 m) lava flows as evidenced from nearside pit and crater walls (Denevi et al., 2012, Robinson et al., 2012), is similar to our lava flow thicknesses (e.g., the layers in strata ***B-C*** and ***D-D′*** are ~2-5 m thick), which match well with Zhinyu crater wall layer thicknesses (Fig. 4). Also, the nearside CE-3 landing site (in mare Imbrium) shows evidence for a similar quiescent period of low volcanic activity that we detail at the CE-4 site between the Imbrian and the Eratosthenian periods.

The formation of intermittent lava flows and a long quiescent period associated with paleo-regolith could relate to factors and processes inside the Von Kármán crater, e.g., the duration of time required for large volumes of melt to collect within the lunar mantle and establish sufficient overburden pressure to erupt on the surface (e.g., Head and Wilson, 2017, Wilson and Head, 2017). However, many challenges remain in understanding the origin of multiple periods of volcanism on the Moon.

4.3. Chronology of strata

Using CSFD (crater size-frequency distribution) measurements, previous work derived an AMA (absolute model age) of 3.15 Ga for a large area of surface mare basalts in Von Kármán crater floor (Pasckert et al., 2018), which corresponds to the area surrounding dome-like units $d1$ and $d2$ and lower elevation areas. We propose this surface layer of mare basalts exposed in the lower elevation areas (i.e. the southern, blue regions in Fig. 6) corresponds to ***D-D′*** (denoted as **Im4**). Crater degradation and burial from younger erosional and depositional events will result in younger than actual CSFD-estimated ages. We thus suggest material in the upper part of **Im4** should be older than 3.15 Ga. Seen from the nearly horizontal strong stripe reflections in ***D-D′***, there may be as many as seven lava flow sub-periods with relatively even eruption intervals. Additionally, a buried lava flow with an AMA of 3.75 Ga, corresponding to the oldest lava flow in our profile ***H-H′*** (**Im1**), was inferred to be an underlying mare deposit in the Von Kármán crater (Pasckert et al., 2018).

4.4. Stratigraphic interpretation of explored region

Three small mare units $u1$, $u2$ and $u3$ (near locations S, P and N, respectively, in Fig. 6) were dated with AMAs of 3.6 Ga, 3.5 Ga and 3.6 Ga, respectively (Huang et al., 2018). The age of 3.6 Ga

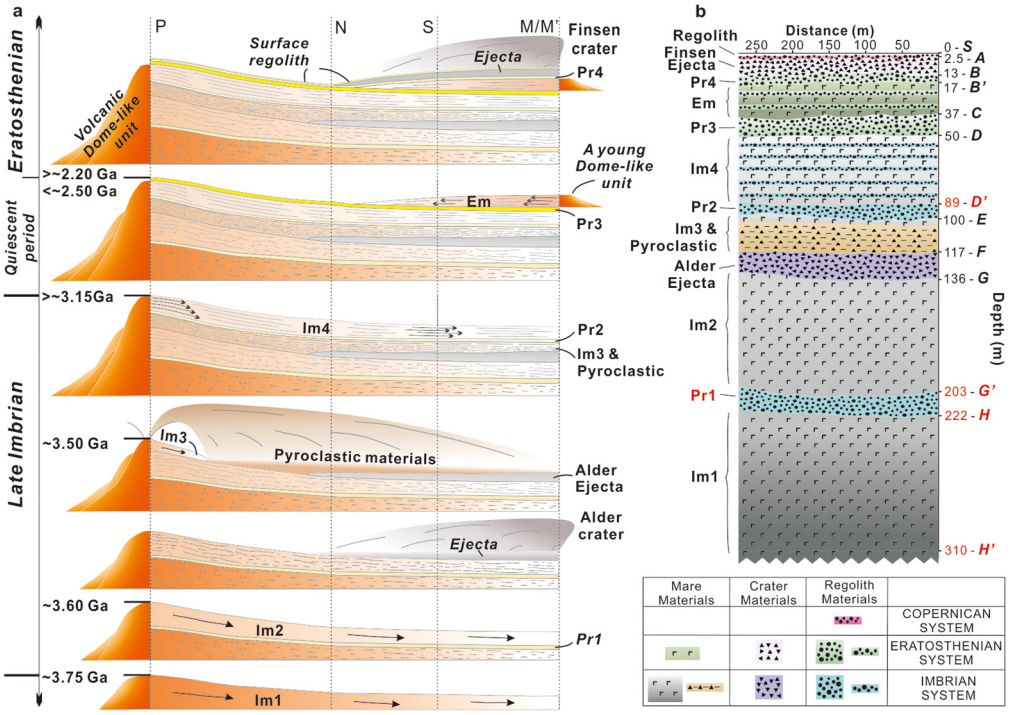

Fig. 7. Possible geological evolution diagram in Von Kármán crater inferred from this study. (a) Geological evolution diagram in Von Kármán crater along the composite Fig. 6 cross-section P-N-S-M (or M') from 3.75 Ga (bottom) to earlier than 2.2 Ga (top), displaying an interpretation for temporal evolution of strata creation. Lunar geologic era names are printed on left, along with ages, and depiction of lava flow dome-like unit evolution (orange "hills", e.g., *d*1 in Fig. 6). Strata include Imbrium lava flows (**Im1**-**4**), paleoregolith layers (**Pr1**-**4**), an Eratosthenian mare unit (**Em**), as well as pyroclastic and ejecta deposits. Arrows indicate inferred mare flow directions. Ages and layer thicknesses are not to scale. The surface regolith was formed after deposition of Finsen crater ejecta. (b) Present day strata interpretation of LPR profiles beneath the Yutu-2 path. Left side symbols correspond to strata interpretations in (a), and right side presents the depths and strata interface letters (from Fig. 3). Text and numbers in red have large uncertainties.

in area *u*1 near point S may be due to old lava flow materials from the north. As area *u*3 near point N has elevations of at least 80 m below surrounding areas (Fig. 6), and the thickness of lava flow deposits generally decreases from their source (presumed to be point P, which is the largest dome-like unit on the western Von Kármán crater floor), we suggest the second oldest period of lava flow deposit ***G***-***G′*** (**Im2**) has the age of ~3.6 Ga. A younger period of volcanic activity may have produced stratum ***E***-***F*** (**Im3**) at ~3.5 Ga (derived from *u*2), where pyroclastic materials were deposited first, then overlaid by a subsequent flow from point P. The Alder ejecta is an episode between the **Im2** and **Im3** flows between 3.15-3.75 Ga—which represents a peak period of volcanic activity within the Von Kármán crater inside SPA basin.

Finally, we construct the possible stratigraphy and evolutionary history of the Von Kármán crater floor based on the LPR strata combined with consideration of the surface geology around CE-4 landing site, as well as in other parts of the Von Kármán crater (Fig. 7). Five periods of large mare basalt flows from regional lava-infilling events were inferred (**Em**, **Im1**, **Im2**, **Im3** and **Im4**). The oldest flow (**Im1**) might have been erupted from a western volcanic vent on the Von Kármán crater floor, forming the deepest imaged Imbrian-aged stratum. After the formation of a paleo-regolith **Pr1**, the second lava flow period occurred from a western source (**Im2**). The Alder crater impact occurred southeast of Von Kármán crater, and deposited a fine ejecta stratum above **Im2**. The third period of volcanism produced a large amount of pyroclastic materials which overlaid the Alder ejecta, followed by a lava flow that covered the surface, forming **Im3**. Subsequent intermittent lava flows with quiescence intervals resulted in **Im4**. Paleo-regolith **Pr2** formed between **Im3** and **Im4**. A quiescent period, with little volcanism and no large impact events, occurred in the Eratosthenian period after the deposition of **Im4**, forming the thick paleo-regolith **Pr3**. This was followed by mare basalts (deposited as unit **Em**) from the eastern Von Kármán crater floor. A thin paleo-regolith **Pr4** subsequently formed on top of **Em**, which was later buried by the ejecta of the Finsen crater from the northeast of Von Kármán crater. Finally, a distinct thin surface regolith formed in our explored area. The southwestern maria regions in Von Kármán crater are expected to have thicker regolith due to the long, continuous formation time. Additionally, the thin surface regolith and **Pr4** are thinner than the early **Pr1**, **Pr2** and **Pr3** events, arguing the impact frequency of small craters, which dominated the regolith deposition rate, has decreased.

4.5. Alternative hypotheses

Here we acknowledge the possibility of other hypotheses to explain the LPR data, as they cannot be fully excluded from current evidence. For example, the **Pr3** may be formed by the Alder ejecta. However, this interpretation appears to have some discrepancies, as very few radial ejecta features can be traced back to the Alder crater, suggesting Alder ejecta deposits have since been buried by the basalts on the southern Von Kármán crater (the blue area in the topographic image in Fig. 6). The topographical elevation of these basalts is more than 60 m lower than that of CE-4 landing site, suggesting that any Alder ejecta should be deeper than **Pr3** when we are assuming all dielectric interfaces are flat-lying with respect to surface topography. **Pr1** should also be a candidate for the Alder ejecta, but its boundaries are vague.

Regarding the young stratum ***B′***-***C***, it can be alternatively interpreted as Imbrain lava materials which corresponds to the first peak of volcanism in SPA. Moreover, the buried 3.75 Ga deposits estimated by Pasckert et al. (2018) may be derived from the shallower layers (e.g., **Im2**, **Im3** or even **Im4**), and then other **Im** units and Alder ejecta would be accordingly older. A challenge with this hypothesis is explaining the homogeneous stratum ***C***-***D***, where a

long hiatus of volcanism in the Von Kármán crater during the Imbrian period is inferred, because lava flows were typically more active in the Imbrian period compared to those in the Eratosthenian period (Haruyama et al., 2009, Pasckert et al., 2018). Concerning the uncertainty of the AMAs calculated from different exposed regions in Von Kármán crater, the exact ages of these strata are only plausible results referred to previous studies (e.g. Huang et al., 2018, Pasckert et al., 2018).

Yutu-2 is still operating on the far side of the Moon, thus additional data will be available to better constrain these geological interpretations.

5. Conclusions

There is good agreement between surface geological features and the structures detected in lunar LPR profiles, supporting the reliability of imaged subsurface structures. Numerous concave and arc shape structures observed at various depths are consistent with buried craters and rocks, indicating that the paleo floor of Von Kármán, as well as the present-day surface, experienced numerous impacting events. The observed strata thicknesses match well with predictions of ejecta thickness from Finsen and Alder craters.

Multiple periods of volcanism are revealed by LPR profiles, which likely originated from dome-like units on the maria floor of Von Kármán. A subsequent younger lava flow unit following the quiescent period provides evidence for young volcanism within Von Kármán. Finally, the most possible stratigraphy and chronology in maria Von Kármán crater within the SPA are constructed, representing an example of evolutionary processes on the farside of the Moon. It is a remarkable fact that some alternative hypotheses cannot be ignored, so more evidence is still needed to constrain and improve our model.

CRediT authorship contribution statement

Yuefeng Yuan: Conceptualization, Funding acquisition, Investigation, Methodology, Writing – original draft. **Peimin Zhu:** Methodology, Supervision, Writing – review & editing. **Long Xiao:** Methodology, Project administration, Writing – review & editing. **Jun Huang:** Data curation, Methodology, Validation. **Edward J. Garnero:** Validation, Writing – review & editing. **Jian Deng:** Data curation, Methodology. **Fenghua Wang:** Investigation, Resources. **Yuqi Qian:** Resources, Software. **Na Zhao:** Data curation. **Wengang Wang:** Visualization. **Weiwei Li:** Visualization.

Declaration of competing interest

The authors declare that they have no known competing financial interests or personal relationships that could have appeared to influence the work reported in this paper.

Acknowledgements

The authors would like to thank the editor W. McKinnon, reviewer B. Thomson and an anonymous reviewer for constructive reviews and comments that helped improve the manuscript. This work was supported by National Natural Science Foundation of China [41904119, 41830214], the Fundamental Research Funds for the Central Universities, China University of Geosciences (Wuhan) [CUG2106109], China Postdoctoral Science Foundation [2018M642950], the Pre-research Project on Civil Aerospace Technologies [D020101] of CNSA, Zhejiang Provincial Natural Science Foundation of China [LQ18A030001], and Ningbo Natural Science Foundation [2019A610090]. Data presented in this paper are hosted at http://moon.bao.ac.cn/index_en.jsp.

Appendix A. Supplementary material

Supplementary material related to this article can be found online at https://doi.org/10.1016/j.epsl.2021.117062.

References

Angelopoulos, M., Redman, D., Pollard, W.H., et al., 2014. Lunar ground penetrating radar: minimizing potential data artifacts caused by signal interaction with a rover body. Adv. Space Res. 54, 2059–2072. https://doi.org/10.1016/j.asr.2013.09.014.

Barker, M.K., Mazarico, E., Neumann, G.A., Zuber, M.T., Haruyama, J., Smith, D.E., 2016. A new lunar digital elevation model from the Lunar Orbiter Laser Altimeter and SELENE Terrain Camera. Icarus 273, 346–355. https://doi.org/10.1016/j.icarus.2015.07.039.

Croft, S.K., 1985. The scaling of complex craters. J. Geophys. Res. 90 (S02), C828–C842. https://doi.org/10.1029/JB090iS02p0C828.

Denevi, B.W., et al., 2012. Physical constraints on impact melt properties from Lunar Reconnaissance Orbiter Camera images. Icarus 219, 665–675. https://doi.org/10.1016/j.icarus.2012.03.020.

Di, K.C., et al., 2019. Chang'e-4 lander localization based on multi-source data. J. Remote. Sens. 23, 177–184. https://doi.org/10.11834/jrs.20199015.

Haruyama, J., et al., 2009. Long-lived volcanism on the lunar farside revealed by SELENE Terrain Camera. Science 323, 905–908. https://doi.org/10.1126/science.1163382.

Head, J.W., Wilson, L., 1992. Lunar mare volcanism: stratigraphy, eruption conditions, and the evolution of secondary crusts. Geochim. Cosmochim. Acta 56, 2155–2175. https://doi.org/10.1016/0016-7037(92)90183-J.

Head, J.W., Wilson, L., 2017. Generation, ascent and eruption of magma on the Moon: new insights into source depths, magma supply, intrusions and effusive/explosive eruptions (part 2: predicted emplacement processes and observations). Icarus 283, 176–223. https://doi.org/10.1016/j.icarus.2016.05.031.

Head, J.W., et al., 1993. Lunar impact basins: new data for the western limb and far side (Orientale and South Pole-Aitken basins) from the first Galileo flyby. J. Geophys. Res. 98, 17,149–17,181. https://doi.org/10.1029/93JE01278.

Hiesinger, H., 2006. New views of lunar geoscience: an introduction and overview. Rev. Mineral. Geochem. 60, 1–81. https://doi.org/10.2138/rmg.2006.60.1.

Housen, K.R., Schmidt, R.M., Holsapple, K.A., 1983. Crater ejecta scaling laws: fundamental forms based on dimensional analysis. J. Geophys. Res., Planets 88, 2485. https://doi.org/10.1029/JB088iB03p02485.

Huang, J., Xiao, Z., Flahaut, J., et al., 2018. Geological characteristics of Von Kármán crater, northwestern South Pole-Aitken Basin: Chang'E-4 landing site region. J. Geophys. Res., Planets 123, 1684–1700. https://doi.org/10.1029/2018JE005577.

Huang, J., Xiao, Z., Xiao, L., et al., 2020. Diverse rock types detected in the lunar South Pole–Aitken Basin by the Chang'E-4 lunar mission. Geology 48, 723–727. https://doi.org/10.1130/G47280.1.

Lai, J., Xu, Y., Zhang, X., Xiao, L., Yan, Q., Meng, X., et al., 2019. Comparison of dielectric properties and structure of lunar regolith at Chang'e-3 and Chang'e-4 landing sites revealed by ground-penetrating radar. Geophys. Res. Lett. 46, 12783–12793. https://doi.org/10.1029/2019GL084458.

Lai, J., Xu, Y., Bugiolacchi, R., et al., 2020. First look by the Yutu-2 rover at the deep subsurface structure at the lunar farside. Nat. Commun. 11, 3426. https://doi.org/10.1038/s41467-020-17262-w.

Li, C., et al., 2018. Pitfalls in GPR data interpretation: false reflectors detected in lunar radar cross sections by Chang'e-3. IEEE Trans. Geosci. Remote Sens. 56, 1325–1335. https://doi.org/10.1109/TGRS.2017.2761881.

Li, C., Su, Y., Pettinelli, E., Xing, S., Ding, C., et al., 2020. The Moon's farside shallow subsurface structure unveiled by Chang'E-4 Lunar Penetrating Radar. Sci. Adv. 6, eaay6898. https://doi.org/10.1126/sciadv.aay6898.

Losiak, A., et al., 2009. A new lunar impact crater database. In: Lunar and Planetary Science Conference.

McGetchin, T.R., Settle, M., Head, J.W., 1973. Ejecta from large craters on the Moon: discussion. Earth Planet. Sci. Lett. 20, 226. https://doi.org/10.1016/0012-821X(74)90115-0.

McKay, D.S., Heiken, G., Basu, A., et al., 1991. The Lunar Regolith. Lunar Sourcebook, vol. 7. Cambridge University Press, Chap, pp. 285–356.

Oberbeck, V.R., 1975. The role of ballistic erosion and sedimentation in lunar stratigraphy. Rev. Geophys. 13, 337–362. https://doi.org/10.1029/RG013i002p00337.

Pasckert, J.H., Hiesinger, H., van der Bogert, C.H., 2018. Lunar farside volcanism in and around the South Pole-Aitken basin. Icarus 299, 538–562. https://doi.org/10.1016/j.icarus.2017.07.023.

Petro, N.E., Pieters, C.M., 2006. Modeling the provenance of the Apollo 16 regolith. J. Geophys. Res. 111, E09005. https://doi.org/10.1029/2005JE002559.

Petro, N.E., Pieters, C.M., 2008. The lunar-wide effects of basin ejecta distribution on the early megaregolith. Meteorit. Planet. Sci. 43, 1517–1529. https://doi.org/10.1111/j.1945-5100.2008.tb01025.x.

Pike, R.J., 1974. Ejecta from large craters on the Moon: comments on the geometric model of McGetchin et al. Earth Planet. Sci. Lett. 23, 265–274. https://doi.org/10.1016/0012-821X(74)90114-9.

Pike, R.J., 1980. Control of crater morphology by gravity and target type-Mars, Earth, Moon. In: Lunar and Planetary Science Conference Proceedings.

Porcello, L.J., et al., 1974. The Apollo lunar sounder radar system. Proc. IEEE 62, 769–788. https://doi.org/10.1109/PROC.1974.9517.

Qiao, L., Ling, Z., Fu, X., Li, B., 2019. Geological characterization of the Chang'e-4 landing area on the lunar farside. Icarus 333, 37–51. https://doi.org/10.1016/j.icarus.2019.05.029.

Robinson, M.S., et al., 2012. Confirmation of sublunarean voids and thin layering in mare deposits. Planet. Space Sci. 69, 18–27. https://doi.org/10.1016/j.pss.2012.05.008.

Russell, J.K., Stasiuk, M.V., 1997. Characterization of volcanic deposits with ground-penetrating radar. Bull. Volcanol. 58, 515–527. https://doi.org/10.1007/s004450050159.

Rust, A.C., Russell, J.K., 2000. Detection of welding in pyroclastic flows with ground penetrating radar: insights from field and forward modeling data. J. Volcanol. Geotherm. Res. 95, 23–34. https://doi.org/10.1016/S0377-0273(99)00119-5.

Sharpton, V.L., 2014. Outcrops on lunar crater rims: implications for rim construction mechanisms, ejecta volumes and excavation depths. J. Geophys. Res., Planets 119, 154–168. https://doi.org/10.1002/2013JE004523.

Simmons, G., Strangway, D., Annan, P., 1973. Surface electrical properties experiment. Apollo 17 Preliminary Science Report. NASA 15, 330.

Stolt, R.H., 1978. Migration by Fourier transform. Geophysics 63, 23–48. https://doi.org/10.1190/1.1440826.

Stuart-Alexander, D.E., 1978. Geologic map of the central far side of the Moon. USGS, map I-1047, 1:5M scale.

Taylor, S.R., 1982. Lunar and terrestrial crusts: a contrast in origin and evolution. Phys. Earth Planet. Inter. 29, 233–241. https://doi.org/10.1016/0031-9201(82)90014-0.

Thomson, B.J., Grosfils, E.B., Bussey, D.B.J., Spudis, P.D., 2009. A new technique for estimating the thickness of mare basalts in Imbrium Basin. Geophys. Res. Lett. 36, L12201. https://doi.org/10.1029/2009GL037600.

Wang, Z., Li, Y., Jiang, J., Li, D., 2010. Lunar surface dielectric constant, regolith thickness, and ^{3}He abundance distributions retrieved from the microwave brightness temperatures of CE-1 Lunar Microwave Sounder. Sci. China Earth Sci. 53, 1365–1378.

Wilhelms, D.E., John, F., Trask, N.J., 1987. The geologic history of the Moon. U.S. Geological Survey Professional Paper 1348.

Wilhelms, D.E., Howard, K.A., Wilshire, H.G., 1979. Geologic map of the south side of the Moon.

Wilson, L., Head, J.W., 2017. Generation, ascent and eruption of magma on the Moon: new insights into source depths, magma supply, intrusions and effusive/explosive eruptions (part 1: theory). Icarus 283, 146–175. https://doi.org/10.1016/j.icarus.2015.12.039.

Xiao, L., Zhu, P., Fang, G., Xiao, Z., Zou, Y., Zhao, J., Zhao, N., Yuan, Y., et al., 2015. A young multilayered terrane of the northern Mare Imbrium revealed by Chang'E-3 mission. Science 347, 1226–1229. https://doi.org/10.1126/science.1259866.

Xie, M., Liu, T., Xu, A., 2020. Ballistic sedimentation of impact crater ejecta: implication for resurfacing and provenance of lunar samples. J. Geophys. Res., Planets 125, e2019JE006113. https://doi.org/10.1029/2019JE006113.

Yingst, R.A., Chuang, F., Berman, D., Mest, S., 2017. Geologic mapping of the Planck quadrangle of the Moon (LQ-29). In: Lunar and Planetary Science Conference. 48 Abstract #1680.

Yingst, R.A., Head, J.W., 1997. Volumes of lunar lava ponds in South Pole-Aitken and Orientale basins: implications for eruption conditions, transport mechanisms, and magma source regions. J. Geophys. Res. 102, 10909–10931. https://doi.org/10.1029/97JE00717.

Yuan, Y., Wang, F., Zhu, P., Xiao, L., Zhao, N., 2020. New constraints on the young lava flow profile in the northern Mare Imbrium. Geophys. Res. Lett. 47, e2020GL088938. https://doi.org/10.1029/2020GL088938.

Yuan, Y., Zhu, P., et al., 2017. The 3-D geological model around Chang'E-3 landing site based on lunar penetrating radar Channel 1 data. Geophys. Res. Lett. 44, 6553–6561. https://doi.org/10.1002/2017GL073589.

Zhang, J., Zhou, B., Lin, Y., et al., 2020a. Lunar regolith and substructure at Chang'E-4 landing site in South Pole–Aitken basin. Nat. Astron. https://doi.org/10.1038/s41550-020-1197-x.

Zhang, L., Li, J., Zeng, Z., Xu, Y., Liu, C., Chen, S., 2020b. Stratigraphy of the Von Kármán crater based on Chang'E-4 Lunar Penetrating Radar data. Geophys. Res. Lett. 47, e2020GL088680. https://doi.org/10.1029/2020GL088680.

Zhao, N., Zhu, P., Yuan, Y., et al., 2018. The shallow subsurface structures of Chang'E-3 landing site based on the wavefield characteristics of LPR Channel-2B data. Adv. Space Res. 62, 884–889. https://doi.org/10.1016/j.asr.2018.05.023.